Meteorol Atmos Phys 93, 97–114 (2006)
DOI 10.1007/s00703-005-0165-4

Meteorology and Atmospheric Physics
Printed in Austria

Joint Center for Earth Systems Technology, University of Maryland, Baltimore County, USA

Variable resolution on quasi-uniform grids: linear advection experiments

M. Rančić and **H. Zhang**

With 15 Figures

Received October 2, 2003; revised September 9, 2005; accepted September 15, 2005
Published online: May 2, 2006

Summary

A couple of different techniques for implementing the variable resolution within numerical models of the atmosphere that use quasi-uniform grids are estimated and compared based on their merit in the simple linear advection experiments. These techniques are: grid stretching, Schmidt transforming and grid overlapping. The quasi-uniform grids are: a conformal cubic and an octagonal grid. The techniques for the variable resolution are evaluated from the perspective of their effects on numerical solution and the practicality of their application. Our analysis suggests that the grid stretching is for now the most optimal choice. However, a special form of grid overlapping is presented that has potential to become a viable alternative in the future.

1. Introduction

Quasi-uniform grids for discretization of the sphere evade well known problems of the standard longitude-latitude grid caused by the convergence of the meridians near the Earth's poles. Randall et al (1998) described the effects of close zonal spacing of grid points near the poles on the longitude-latitude grid as an ''excessive spatial resolution'', which does not effectively exploit computer resources. Typically, the areas around poles are first over-resolved, wasting memory, and then the impact of this over-resolution is removed through polar filtering, wasting the computer time as well. This is particularly inconvenient on the contemporary distributed memory computers, because the filtering operators tend to increase the amount of inter-processor communications, and, being applied only to the areas around poles, produce a computational imbalance. Quasi-uniform grids on the other hand offer a high degree of spatial isomorphism and represent an attractive alternative.

Following early papers of Sadourny et al (1968), Williamson (1970), and Sadourny (1972), a number of authors in the last decade or so became interested in the development and application of quasi-uniform spherical grids. These grids are in the most cases derived by a spherical expansion of different polyhedrons, that is, a central projection from the center of a polyhedron to the sphere circumscribed around it. Quasi-uniform grids may be roughly classified in two main groups, depending on the structure of the basic grid element. They may be *triangular* (e.g., Baumgardner and Frederickson, 1985; Ničković, 1994; Heikes and Randall, 1995a and b; Ničković et al, 2002; Majewski et al, 2002, Tomita et al, 2002) or *rectangular* (e.g., Ronchi et al, 1996; McGregor, 1997; Taylor et al, 1997; Adcroft et al, 2004). Grids with the *triangular* basic element may imply an *octahedral*, *icosahedral*, *dodecagonal* or *tetrahedral* spherical

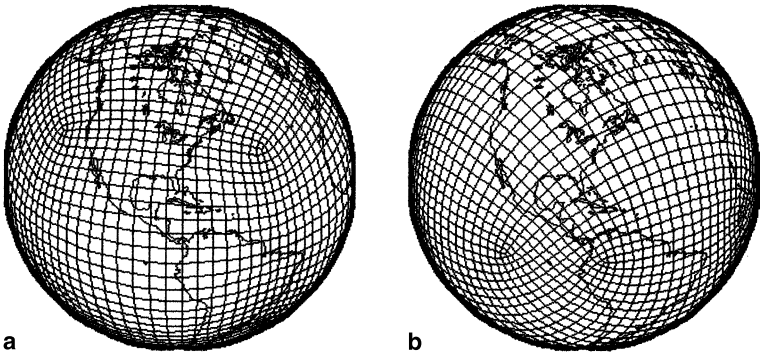

Fig. 1. Conformal cubic (**a**), and octagonal (**b**) spherical grids

expansion. The *rectangular* grids may also include a variety of different topologies, though all the works quoted above actually deal with an e*xpanded spherical cube*.

In this paper we will consider two special rectangular, nearly conformal, quasi-uniform grids: *cubic* (Rančić et al, 1996) and *octagonal* (Purser and Rančić, 1997), which are respectively shown in Fig. 1a and b.

The conformal cubic grid is defined by a conformal transformation that numerically generates coordinates on the faces of the spherical cube. Coordinate lines smoothly pass across the edges, avoiding an angular discontinuity that otherwise would exist on the spherical cube. *The conformal octagonal* grid is derived following the same concept, with eight singular (corner) points removed from the mid latitudes and arranged along the equator.

The major objective of the paper is to evaluate different strategies for implementation of the variable resolution on the cubic and octagonal grids.

One of the reasons for exploring the variable resolution is to find a more efficient alternative for the classical sequential paradigm of the short range weather forecast in which a high-resolution regional model typically relies on, and has to follow up, the integration of a separate, low-resolution global model. Usually, the regional and the global models have different numerical approximations and physical parameterizations, which may adversely reflect on the performance of the regional model and there is no feedback from the high-resolution regional to the driving global model.

Another area for application of the variable resolution is the regional climate downscaling (e.g., Takle et al, 1999). These are typically very long-time integrations in which a regional model is forced through its lateral boundaries by a low resolution climate model. There is a concern that with progressing of time, the abrupt difference in numerical propagation speeds of weather patterns that exists in the global and the regional model because of their different resolutions may become one of the predominant sources of errors in these experiments. The variable resolution appears to be in this situation a viable alternative (e.g., Deque and Piedelievre, 1995; Fox-Rabinovitz, 2000).

The technique of *grid stretching* represents presently the most extensively used method for including the variable resolution in numerical models of the atmosphere. Typical grid stretching consists of a smooth and gradual increase of density of the coordinate lines over specific locations of interest. The topology of the integration domain remains identical as in the case of the non-stretched grid and there is no discontinuity of the grid lines. An equal amount of grid stretching applied in both horizontal directions (and throughout the whole integration domain) provides a symmetrical change of dispersion properties around the high-resolution portion of the grid and prevents deformation of the numerical solution. So far, the grid stretching has been mainly used in the context of classical spherical longitude-latitude grid (e.g., Côté et al, 1993; Fox-Rabinovitz et al, 2001, and the literature cited there). In this paper, the technique of grid stretching will be tested in the context of the rectangular, conformal, quasi-uniform grids.

Another approach that will be considered in this paper is *asymmetric mapping*, usually referred to as a Schmidt (1977) transformation. This is an alternative way to continuously locally enhance the grid resolution. Instead of directly changing the density of the coordinate lines,

we perturb the symmetry of the underlying grid topology, which then in turn produces the effect of stretching. A version of the Schmidt transformation that was developed for the octagonal grid by Purser and Rančić (1997) will be in this paper carefully compared against grid stretching.

The third technique that will be to some extent explored in this paper is a method of *grid overlapping*. The grid overlapping (e.g. Starius, 1980; Chesshire and Henshaw, 1990) is a technique in which the numerical solution is allowed to propagate between different, mismatched grids via a common overlapping area. The solutions from different grids are brought together through the use of the high-order interpolations and then are coupled by the weight averaging. In comparison to grid stretching, grid overlapping deals only with the regularly spaced grids and avoids the local anisotropy of the grid elements. Examples of early applications in the atmospheric science may be traced back to Phillips (1959), and Browning et al (1989).

Our goal is to evaluate relative merits of these techniques in application on the quasi-uniform grids in a series of tests with the increasing level of complexity. This paper presents an initial set of linear advection experiments in which we try to establish the preliminary idea about the relative behavior of these techniques and develop necessary numerical infrastructures. In all tests we use the Takacs (1985) linear advection scheme which is third-order accurate on the non-stretched grids and applies directional splitting of Strang (1968) to access the multidimensional case. Along the way we address the issue of how the singular points on the quasi-uniform grids may adversely affect numerical solution of directionally split schemes, and we suggest a solution to this problem.

Section 2 presents the numerical scheme that will be used in the various tests throughout the paper and shows the results of advection tests in the plane. The results of test integrations on the conformal cubic and octagonal grids and the new technique for treatment of the singular points are given in Sect. 3. Section 4 finalizes with the discussion and conclusions.

2. Tests on the plane

The purpose of tests in the plane is to explore and to compare different techniques for the variable resolution in the simplest possible context and to develop a general framework for the algorithms that will be applied on the quasi-uniform grids. We consider both methods of the grid stretching and the grid overlapping in these tests.

In the one-dimensional (1D) case we numerically solve the linear advection equation:

$$\frac{\partial \psi}{\partial t} + c\frac{\partial \psi}{\partial x} = 0. \tag{1}$$

Here, ψ is an advected quantity, c is a constant velocity of the flow in the x-direction, and t is time.

The finite-difference scheme Takacs (1985) is in the case of constant flow at the variable resolution defined by

$$\begin{aligned}\psi_j^{n+1} = \psi_j^n &- \frac{\mu_j}{2}(\psi_{j+1}^n - \psi_{j-1}^n) \\ &+ \frac{\mu_j^2}{2}(\psi_{j+1}^n - 2\psi_j^n + \psi_{j-1}^n) \\ &- \frac{(1+\mu_j)\mu_j(\mu_j-1)}{6}(\psi_{j+1}^n - 3\psi_j^n \\ &+ 3\psi_{j-1}^n - \psi_{j-2}^n).\end{aligned} \tag{2}$$

The scheme is third-order accurate in the case of uniform resolution. Here, the superscripts n and $n+1$ denote successive time levels, and subscripts $j-2, j-1, j, j+1$ denote locations in space; $\mu_j = c\Delta t/\Delta x_j$ is the Courant number; Δt and is the time-step and Δx_j is the variable grid interval defined at the same locations as the scalar ψ.

In the general flow case at the variable grid, Takacs scheme may be written using a mass conservative flux form of a predictor-corrector sequence:

Predictor:

$$\psi_j^* = \psi_j^n - \frac{1}{\Delta x_j}[F_{j+1/2} - F_{j-1/2}]. \tag{3}$$

Here

$$F_{j+1/2} = \gamma_{j+1/2}^{+}\psi_j^n + \gamma_{j+1/2}^{-}\psi_{j+1}^n, \tag{4}$$

$$\gamma_{j\pm 1/2} = c_{j\pm 1/2}\Delta t, \quad \gamma_{j+1/2}^{\pm} = \left(\frac{\gamma \pm |\gamma|}{2}\right)_{j+1/2}.$$

Corrector:

$$\begin{aligned}\psi_j^{n+1} = \psi_j^n - \frac{1}{\Delta x_j}\Bigg\{&\frac{1}{2}[P_{j+1/2} - P_{j-1/2}] \\ &- \left[\alpha_j^1 Q_{j+1/2} - \alpha_j^2 Q_{j-1/2}\right]\Bigg\}.\end{aligned} \tag{5}$$

Here

$$P_{j+1/2} = \gamma^{+}_{j+1/2}(\psi^{*}_{j+1} + \psi^{n}_{j}) + \gamma^{-}_{j+1/2}(\psi^{*}_{j} + \psi^{n}_{j+1}), \tag{6}$$

$$\begin{aligned} Q_{j+1/2} = & [\gamma^{+}_{j+1/2}(\psi^{*}_{j+1} - \psi^{n}_{j}) \\ & - \hat{\gamma}^{+}_{j+1/2}\hat{\gamma}^{+}_{j-1/2}(\psi^{*}_{j} - \psi^{n}_{j-1})] \\ & - [\gamma^{-}_{j+1/2}(\psi^{n}_{j+1} - \psi^{*}_{j}) \\ & + \hat{\gamma}^{-}_{j+1/2}\hat{\gamma}^{-}_{j+3/2}(\psi^{n}_{j+2} - \psi^{*}_{j+1})] \end{aligned} \tag{7}$$

and

$$\alpha^{1,2}_{j} = \left(\frac{1 + |\mu^{1,2}_{j}|}{6}\right), \qquad \hat{\gamma}^{\pm}_{j} = (|\gamma^{\pm}_{j}|)^{\frac{1}{2}}.$$

The variable Courant number is here defined as

$$\mu^{1}_{j} = \frac{\gamma_{j+1/2}}{\Delta x_j}, \qquad \mu^{2}_{j} = \frac{\gamma_{j-1/2}}{\Delta x_j}. \tag{8}$$

We assume a staggered grid distribution, where the winds are separated from the scalar points and defined in the middle of scalar grid boxes, at locations denoted as $j \pm 1/2$. This formalism is slightly different from the original Takacs (1985) formulation, and is derived by a consistent application of the variable resolution assumption. In our tests the scheme did not work well without these modifications. It should be pointed out that the strict third-order of accuracy is lost on the stretched grid. However, using a moderate stretching is beneficial for keeping the accuracy (not order) under control. Also, the described staggering of the variables results in the increase of the effective resolution, which compensates for the loss of the order.

In the two-dimensional (2D) case on the plane we solve equation:

$$\frac{\partial \psi}{\partial t} = -\left(c_x \frac{\partial \psi}{\partial x} + c_y \frac{\partial \psi}{\partial y}\right). \tag{9}$$

Here, c_x and c_y are components of a constant wind in the x- and y-direction, respectively. Takacs

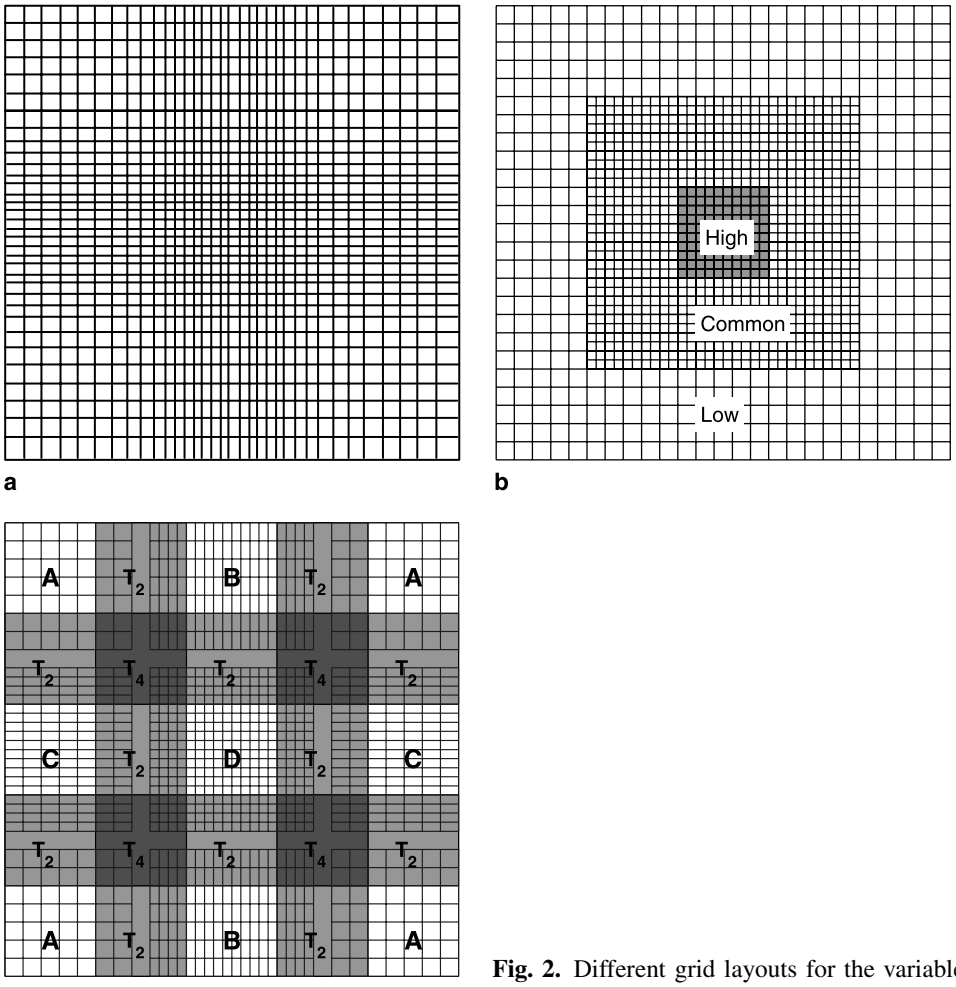

a b c

Fig. 2. Different grid layouts for the variable resolution. (**a**) Stretched grid, (**b**) overlapped grid (version 1), (**c**) overlapped grid (version 2)

(1985) scheme is applied in 2D case through directional splitting, that is, two successive applications of 1D operator defined in (3)–(8). Arakawa C-grid is used in all experiments as the most convenient distribution of variables for a 2D generalization of Takacs scheme.

Besides a uniform grid, with the domain size of 100×100 nondimensional units, three other grids at a variable resolution are used in the tests: one *stretched* and two *overlapped* (shown in Fig. 2a–c). Note that though we use customary term ''stretch'' to describe the grid with the continuously increased resolution, we actually do not ''stretch'' the resolution but instead add new grid points.

Two low-resolution regions on the *stretched grid* are located from 0 to 20 and from 80 to 100 units in each direction. The high-resolution region is defined between 40 to 60 units and the transitional regions with the linear change of the resolution range from 20 to 40 and from 60 to 80 units, respectively in each direction. The *global stretching factor*, (or just stretching factor) defined as the ratio between the largest and the smallest grid distance, is set to 2. The *local stretching factor*, defined as a percent rate of the local increase between two adjacent grid distances in the transitional region, is 2.5%. The total number of grid points is 18,225.

Two settings are available for the construction of the *overlapped grid. Version 1* (shown in Fig. 2b) is generated by overlapping a low-resolution grid that covers entire domain except the central are with x, $y \in [40, 60]$, and a high-resolution grid located in the central area x, $y \in [20, 80]$, where numbers in the brackets refer to nondimensional units. The domain that is covered by both grids is the *overlapping region*. In our case the overlapping region frames the central high resolution area with the width of 20 units which is the same as the width of the transitional region on the stretched grid. The grid interval is 1.0 in the low-resolution and 0.5 in the high-resolution region. The total number of grid points is 24,481.

The second layout for the overlapping grid (*version 2*) is more complicated. In a way, it more closely emulates the layout of the stretched grid with a series of regularly spaced grids. Version 2 consists of four different types of regions with uniform resolution as shown in Fig. 2c. Type A has the low resolution in both x- and y-directions. Type D has the high resolution in both x- and y-directions. Type B has the high resolution in the x- and the low resolution in the y-direction, while the type C has the high resolution in the y-direction and the low resolution in the x-direction. Similarly, there are two types of the overlapping areas: those with two (T_2 in the figure) and those with four (T_4 in the figure) grids covering the same area. In our tests, the size and resolution of domains (A, B, C, and D) and the overlapping areas (T_2 and T_4) are chosen consistently with the first overlapping layout and with the stretched grid (that is, the size of domains is 20×20 units, and the high resolution has grid size 0.5). In this way, all three layouts make a consistent framework. The total number of grid points at this overall layout is 41,209.

In the 1D case, values in the overlapping areas are updated according to formula:

$$\psi^{\text{new}}_{L(H)} = \alpha \psi^{\text{old}}_{L(H)} + (1 - \alpha)\tilde{\psi}_{H(L)}. \tag{10}$$

Here, $\psi^{\text{old}}_{L(H)}$ is the value within the overlapping area of one of the low-resolution regions (or high-resolution) before mixing; $\psi^{\text{new}}_{L(H)}$ is the new value after mixing and $\tilde{\psi}_{H(L)}$ is the value at this same location derived by interpolation from the high (or one of the low-resolution) region. In this paper, we use the 5th-order Lagrangian interpolations. The weight factor α is a nonlinear function of a nondimensional distance ς

$$\alpha = \frac{1}{2}\left[1 + \frac{4}{\pi}\arctan\varsigma\right]. \tag{11}$$

Here, $\varsigma = (2x - x_l - x_r)/(x_r - x_l)$, where x_l and x_r are the coordinates of the left and the right boundary of the coupling region, respectively. When applied to the low resolution, α is equal to 0 at the ends of the overlapping areas toward the high resolution and to 1 at the opposite ends. In principle, the same method applies to the high-resolution solution, with the different orientation of distance ς. In our tests we further refine this technique by imposing that only a portion (p) of the high-resolution grid points in the overlapping area located near the boundary uses the described method for coupling from the low to the high resolution. When p is equal 1, the coupling is symmetrical. When p is 0, the low resolution domain provides only end boundary conditions for the high resolution domain. In this way we enforce an asymmetric interaction between

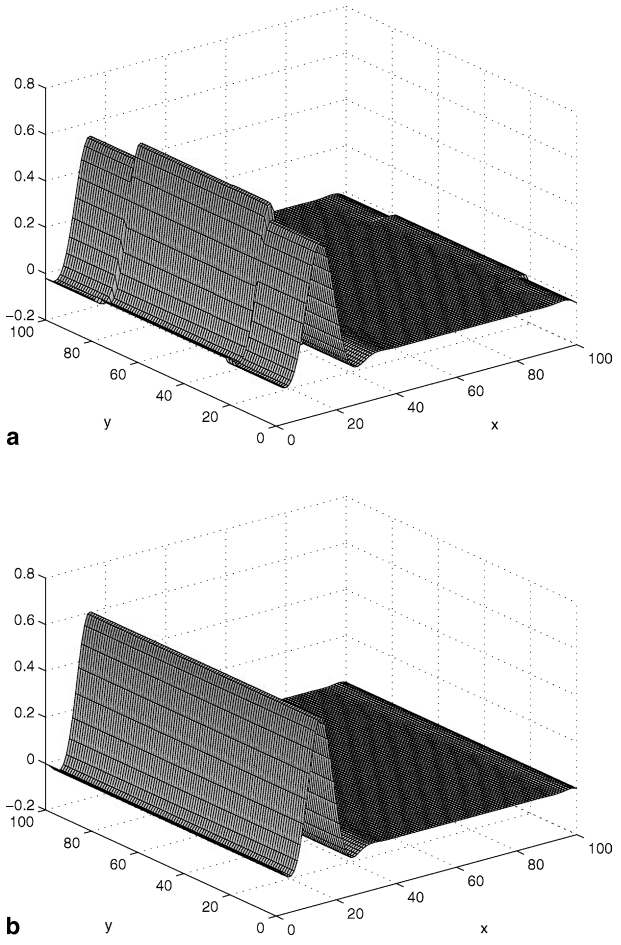

Fig. 3. Shape of the wedge after 5 rotations in the normal direction: (**a**) Version 1 of the overlapped grid, (**b**) version 2 of the overlapped grid

differently resolved areas, that is, a stronger influence from the high on the low resolution than vice versa. In 2D case, the mixing ratios are first calculated for each direction separately, and then multiplied in order to get the final value.

We designed an experiment in which a wedge-shaped scalar perturbation with unit height and base of 10 units is translated at a constant wind. Two series of tests have been performed with the translation in the normal direction (at the speed equal to 1.0) and in the diagonal direction (at speed equal to 1.41). The time-step in all tests is 0.2. Periodic boundary conditions are applied.

The solutions after 5 translations in the normal x-direction on two different overlapped grids are shown in Fig. 3a, b. The shape of the version 1 of the overlapped grid has larger amplitude in the center, and smaller amplitude outside as a consequence of different numerical dispersions. This is effectively avoided by the layout of version 2 of the overlapped grid. The solution on the stretched grid has a very similar shape as the solution on the version 2 of the overlapped grid, with the uniform amplitudes in the y-direction.

The diagnostics l_1 is calculated in all tests, except for the version 1 of the overlapped grid, which is clearly inferior as discussed above. It is defined following Williamson et al (1992) as

$$l_1 = \frac{\int |\psi - \psi_T| dx}{\int |\psi_T| dx}. \tag{12}$$

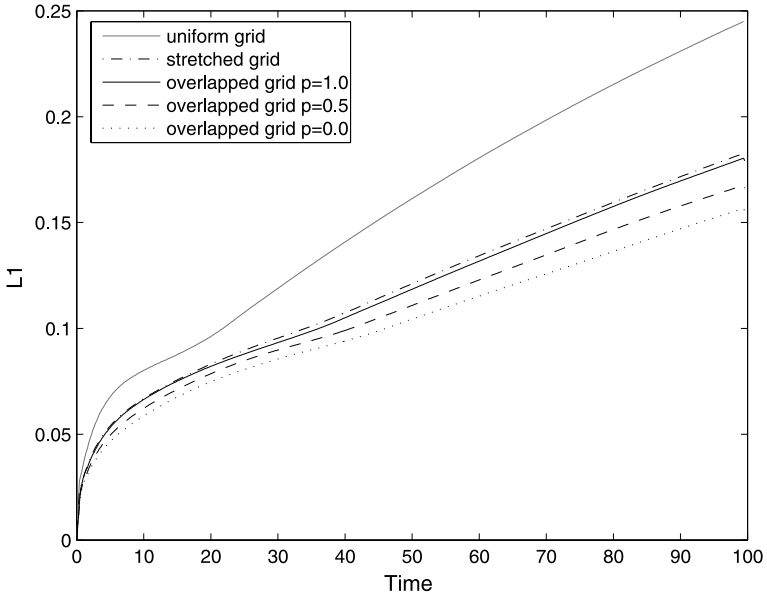

Fig. 4. Diagnostics l_1 in 2D tests on the plane with translation in the diagonal direction

Here ψ is a numerical solution and ψ_T is an analytic (true) solution. In the overlapping areas l_1 is evaluated from the low-resolution solution.

The diagnostics generated in the diagonal tests are shown in Fig. 4. This result is somewhat better than the one in the normal direction because of the implied higher resolution. The smallest resolvable wave in the diagonal direction is $\sqrt{2}/2$ shorter than that in the normal direction (e.g., Mesinger and Arakawa, 1976). The stretched grid improves the results in comparison to the uniform grid, though it performs systematically somewhat worse in comparison to the tests on the version 2 of the overlapped grid. In the absence of formal wave analysis, we speculate that this is a consequence of the local anisotropy of resolution on the stretched grid.

Based on these results, we draw three major conclusions: (1) stretched grid improves the solution; (2) version 2 of the overlapping grid is in the context of our tests generally somewhat better than that of the stretched grid; (3) version 1 of the overlapped grid is not a good candidate for the local enhancement of resolution.

Based on the format of these tests and judging only by the performance, it appears that the version 2 of the grid overlapping should be the technique of choice for the variable resolution. However, the total number of grid points on the overlapping grid is much higher than on the stretched grid, which means that the overlapping grid consumes more computing memory. Also, there is a computational overhead involved in coupling the solutions on the overlapping grid, and, related to this, an increased amount of communications among processors on a contemporary distributed memory computer. And finally, but not completely insignificant, coding on the overlapping grid is more complicated and time consuming.

Because of all of these reasons, we decided to proceed only with the grid stretching in this paper. However, we note that the version 2 of the grid overlapping, in spite of all mentioned problems, should not be overlooked, because of its potential to deliver better numerical solution.

3. Tests on quasi-uniform grids

The coordinate lines on a quasi-uniform grid are not orthogonal and hence the general curvilinear coordinate system needs to be applied in order to describe the scalar equations of motion (e.g., Sadourny, 1972; Rančić et al, 1996). Within this system, the base vectors are defined as

$$\mathbf{a}_1 = \frac{\partial \mathbf{R}}{\partial x}, \quad \mathbf{a}_2 = \frac{\partial \mathbf{R}}{\partial y}, \tag{13}$$

where $\mathbf{R}$ denotes the vector of the absolute Cartesian coordinates (X, Y, Z).

Wind vector can be expressed in terms of *contravariant* ($\tilde{u}$, $\tilde{v}$) and *covariant* components (u, v). Here, only contravariant components are relevant for the linear advection test, and they are defined by

$$\mathbf{V} = \tilde{u}\mathbf{a}_1 + \tilde{v}\mathbf{a}_2. \tag{14}$$

Metric coefficients of the transformation are defined by the scalar product of the base vectors:

$$q_{ij} = \mathbf{a}_i \cdot \mathbf{a}_j \quad i,j = 1,2. \tag{15}$$

The absolute value of the Jacobian of metric coefficients, G, is proportional to the surface element on the sphere:

$$G \equiv |\mathbf{a}_1 \times \mathbf{a}_2| = \sqrt{Det(q_{ij})} = dS/(dxdy). \tag{16}$$

A more detailed description of general curvilinear coordinates can be found, for example, in the classical textbook by Fletcher (1991).

The flux form of the advection equation can be written in the general curvilinear system as

$$\frac{\partial \psi}{\partial t} = -\frac{1}{G}\left\{ \frac{\partial (G\tilde{u}\psi)}{\partial x} + \frac{\partial (G\tilde{v}\psi)}{\partial y} \right\}. \tag{17}$$

As in the tests on the plane, we use the directional splitting and a C-grid version of Takacs (1985) scheme for numerical integration. The layout of the C-grid is chosen so that the wind components are located on the edges of the faces pointing across the edges (that is, $\tilde{u}$-component along vertical edges, aligned with the y-axis, and $\tilde{v}$-component along horizontal edges, aligned with the x-axis), so that there are no grid points defined at the corners. Formulas in Eqs. (3)–(8) describing the advection scheme remain the same, but Δx_j is now replaced by G, and instead of c_x and c_y we now use $\tilde{u}G$ and $\tilde{v}G$, respectively.

Two linear advection tests are performed, in which a perturbation of a passive scalar is rotated around the sphere. In the first one, proposed as a benchmark by Williamson et al (1992), a cosine bell of a passive scalar is advected at the rate of

one rotation per 12 days. In the second one, the cosine bell is replaced with a cosine wedge, but the same wind field is used. This test is applied only on the octagonal grid. In both tests, the analytical solution consists of the initial perturbation that rotates without change of the shape.

A set of diagnostics proposed in Williamson et al (1992) is calculated and graphed as function of time. These diagnostics are: normalized global errors: l_1, l_2, l_∞, normalized mean, variance, and maximum and minimum difference between analytical and numerical solution.

We will first present the problem related to the singular corners on the quasi-uniform grids, and then the results of test integrations on the cubic and octagonal grid.

3.1 A "corner problem" on the quasi-uniform grids

Both the cubic and the octagonal grid have eight unique, singular points that break general isotropy of the grid structure. The uniqueness of the singular (or "corner") points is expressed

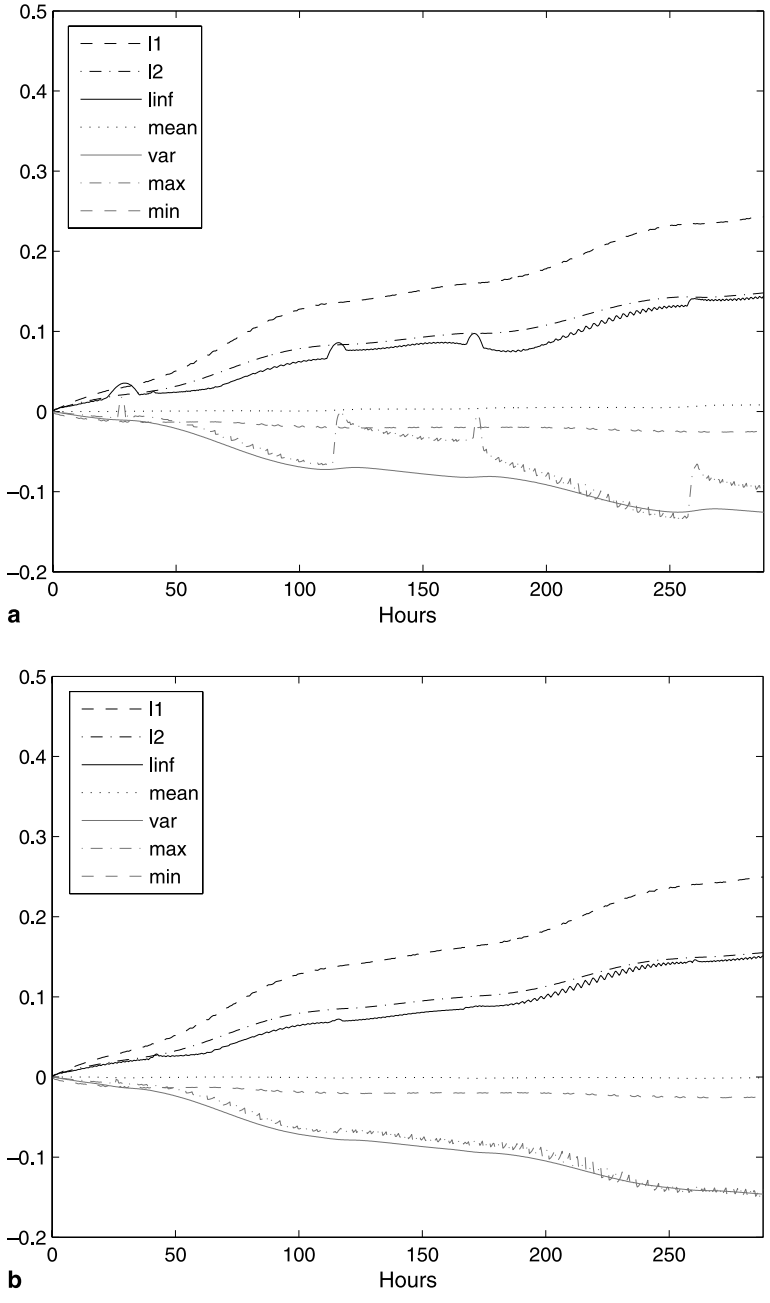

Fig. 5. Diagnostics derived in the rotational test on the cubic grid when perturbation moves across the corners: (**a**) before, (**b**) after applying modification

not only by the different number of grid boxes that surround a grid point (3 instead of 4 as elsewhere) but also by the irregularity of the size and shape of the grid boxes in the vicinity of the corners.

A typical mechanism of the false forcing near the corners is discussed in more details in the Appendix. The linear advection experiment on the cube is used here to illustrate the essence of the problem. The direction of the rotation is chosen so that perturbation first moves diagonally across one face of the cube, goes along the edge of two neighboring faces, and then finishes its path in the identical manner on the opposite side of the cube. In this way, the perturbation has to pass across 4 corners. The diagnostics derived in this test are shown in Fig. 5a.

Two "bumpy" diagnostics, $l_{\inf}$ and $e_{\max}$, are defined as

$$l_{\inf} = \frac{\mathrm{Max}|\psi - \psi_T|}{\mathrm{Max}(\psi_T)},$$
$$e_{\max} = \frac{(\mathrm{Max}(\psi) - \mathrm{Max}(\psi_T))}{(\mathrm{Max}(\psi_T) - \mathrm{Min}(\psi_T))}. \quad (18)$$

They are both related to the peak of the perturbation. The bumpiness expresses the fact that while crossing over the corners, the numerical solution experiences a sudden change (gain) of the maximum value. Most of other diagnostic variables are related to the average values and therefore do not react that much to the extreme local forcing as $l_{\inf}$ and $e_{\max}$.

A new technique is applied in this paper in order to solve the problem. The grid is modified in such a way as to enforce parallelism of the sides of grid boxes near the corners. This technique at the same time reduces a sudden change of resolution, but produces a small overlapping of the three neighboring faces across the corners. The modified grid is shown in Fig. 6.

Only four grid boxes surrounding the corner (as shown in the picture) are modified on the "visible part" of the face. New grid boxes are successively formed by requiring that two sides of a box that lay closer to the corner become parallel to the two opposing sides that remain fixed. For example, using notation from Fig. 6, we first modify sides c_1 and b_1 of the box **A**, in such a way that they become parallel to the sides c_0 and b_0, respectively. Furthermore, we modify

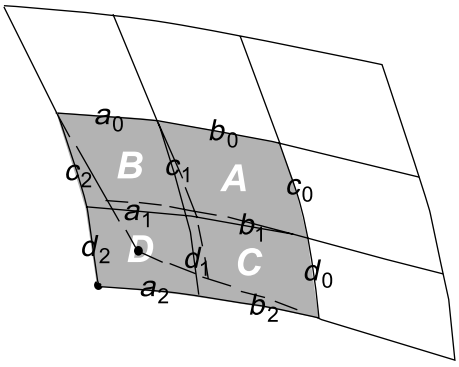

Fig. 6. Modified conformal quasi-uniform grid near the lower-left corner

sides c_2 and a_1 of the box **B**, and sides d_1 and b_2 of the box **C**, so that they become parallel to the opposing sides c_1 and a_0, that is, d_0 and b_1, respectively. Finally, we modify sides d_2 and a_2 of the box **D**, so that they become parallel to the sides d_1 and a_1 derived in the previous iteration. Additional grid boxes close to the corners within the "invisible part" or "halo" of a face (the space from which come the boundary conditions) are constructed in the similar way, so that now the corner box loses its uniqueness and becomes equal to all other grid boxes in the domain. This method increases the size of the smallest grid boxes around singularities. However, each face is now overlapping with two other neighboring faces across the corners, and we need to interpolate and exchange values between the overlapping areas. We use here the simplest, linear interpolations, taking advantage of the close proximity of the grid points involved in the interpolations. The overall amount of overlapping (and consequently the computational overhead) is actually very small and limited to just several grid boxes around the corners. Out of the modified grid boxes, coordinate lines smoothly flow from one face of the cube/octagon to another.

The results of the rotational test over the corners on the modified cubic grid are shown in Fig. 5b. The "bumps" are now completely removed. Similar results are derived on the octagonal grid.

3.2 Variable resolution on the cubic grid

The uniform cubic grid that is used in the control tests has 40×40 grid points on each face, totaling to 9,600 grid points on the whole sphere. This

is rather a small resolution in comparison to the prevailing resolutions of the contemporary global models, but it may faster reveal the nature of the potential problems. The time-step in all experiments is 10 min.

Grid stretching is applied on two opposing faces of the cubic grid. On each of these two faces the same portion of the domain is covered with the low resolution, high resolution and the transitional areas, exactly as it was done in 2D tests on the plane. On the remaining four faces, the grid lines are automatically stretched only in one direction and stay uniform in another. The grid spacing on the low-resolution is the same as on the uniform grid. The global stretching factor is equal to 2, and the local stretching is 6%. Figure 7 shows a face of the cubic grid on which the stretching is applied in both directions.

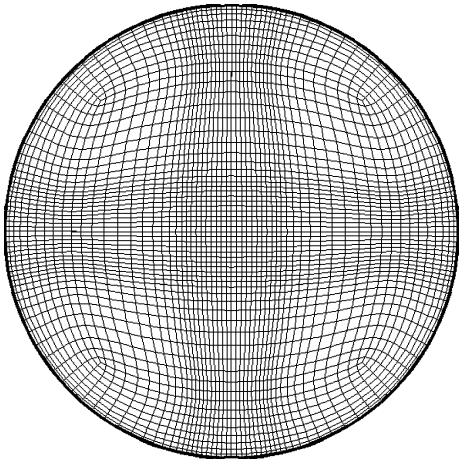

Fig. 7. Stretched cubic grid

In the control run in the *normal* direction, the cosine bell propagates across the middle of 4 faces, passes across 4 edges and returns back to its original position. Figure 8 shows the diagnostics generated in this test. The slight waving of the curves is a consequence of increase of the resolution near the edges of the conformal cube.

Rotation in the normal direction on the stretched grid is done in two different ways. In the first test the perturbation moves across both faces which have resolution enhanced in two directions (as shown in Fig. 7). In the second test the perturbation is going around the cube effectively avoiding these two faces. However, note that precisely in this second trail the perturbation is passing over 4 areas where the resolution is *enhanced in the direction of propagation*! Thus, in a way, this second test emulates the situation in which all 6 faces on the cube would have locally enhanced resolution. Diagnostics generated in these two tests are shown in Fig. 9a and b, respectively.

As before, the grid stretching significantly improves overall performance. The results are especially better in the case of advection over 4 areas with the high resolution in the direction of propagation, as one may expect.

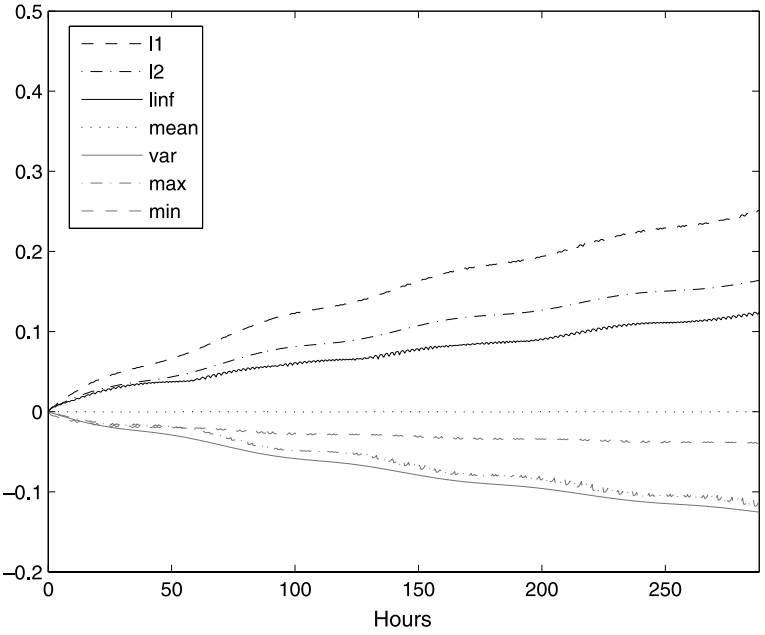

Fig. 8. Diagnostics of the cosine bell test on the cubic grid with uniform resolution (normal direction of rotation)

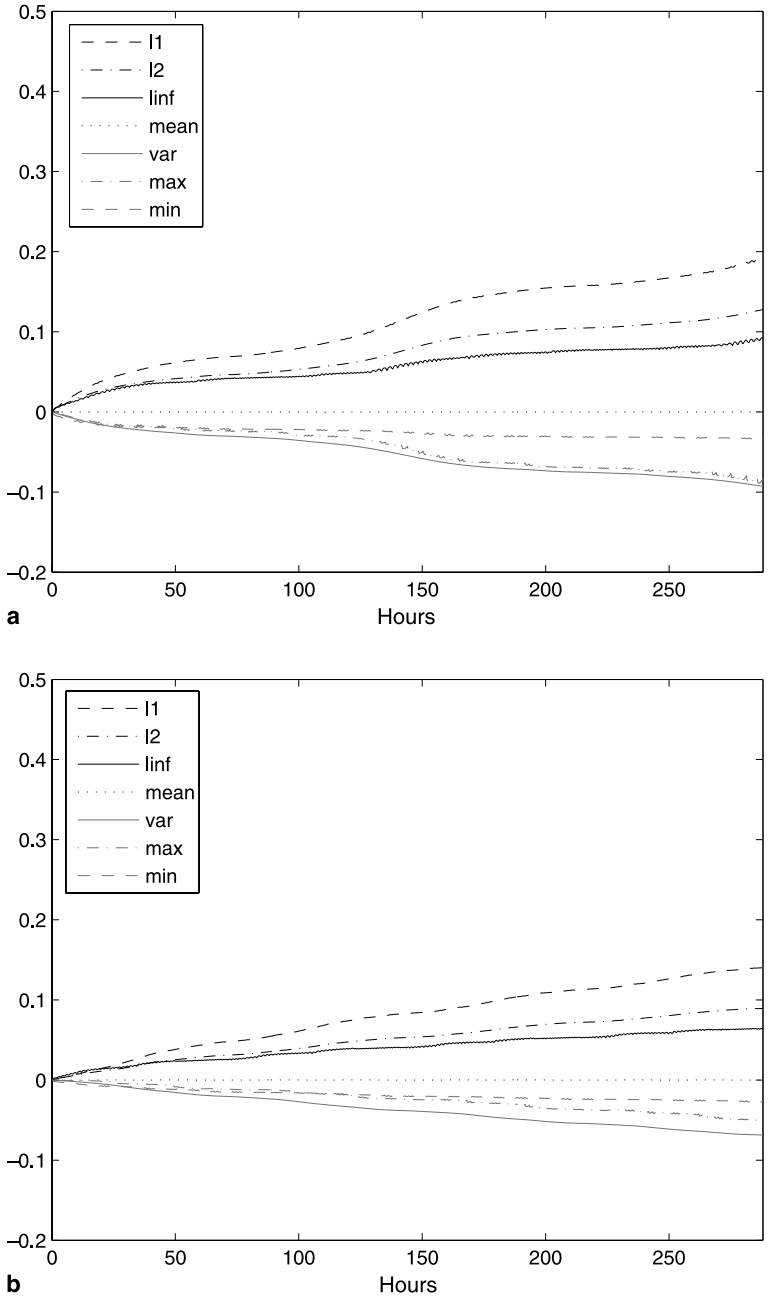

Fig. 9. As in Fig. 8, but for the stretched grid with perturbation passing over (**a**) 2, (**b**) 4 areas with the high resolution in the direction of propagation

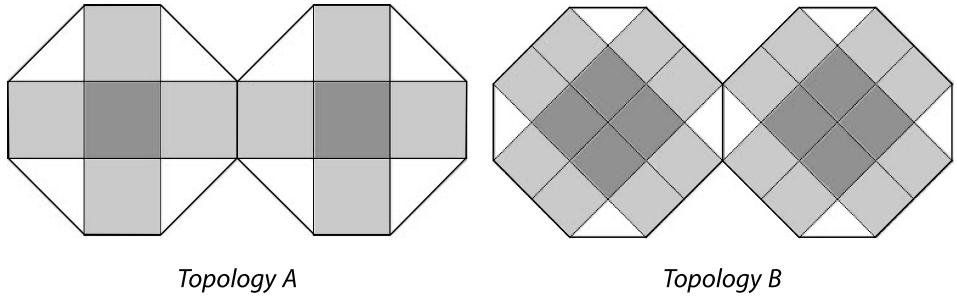

Fig. 10. Two different topologies for the octagonal grid

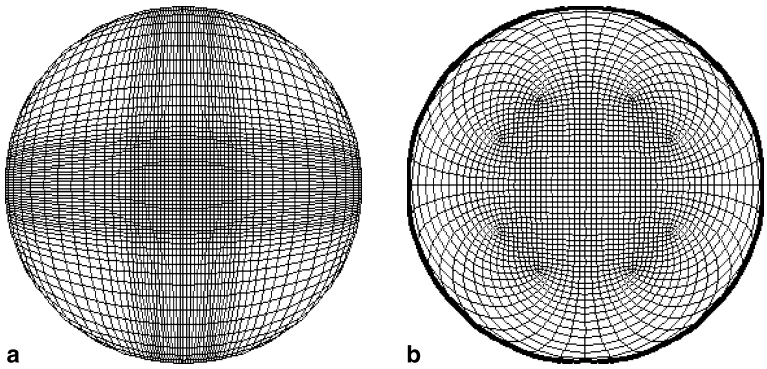

Fig. 11. Octagonal grid with variable resolution: (**a**) stretched, (**b**) Schmidt transformed

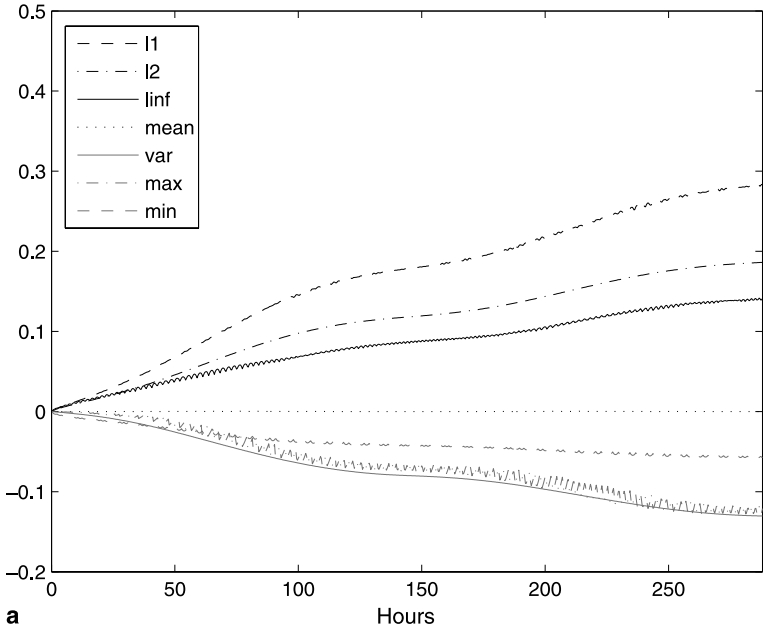

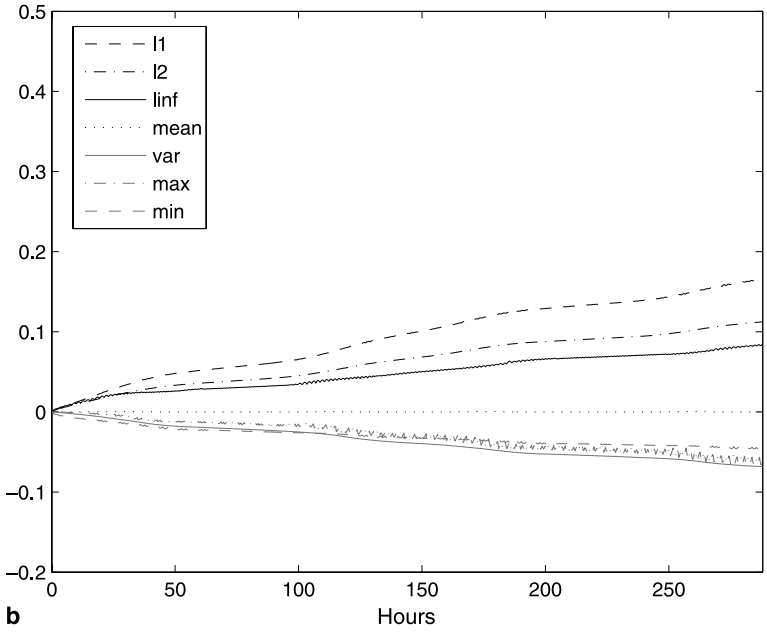

Fig. 12. Diagnostics in the cosine bell test on the octagonal grid: (**a**) uniform resolution, (**b**) stretched grid with the stretching factor 2.0, (**c**) stretched grid with the stretching factor 8.0, (**d**) Schmidt-transformed grid with the stretching factor 2.0

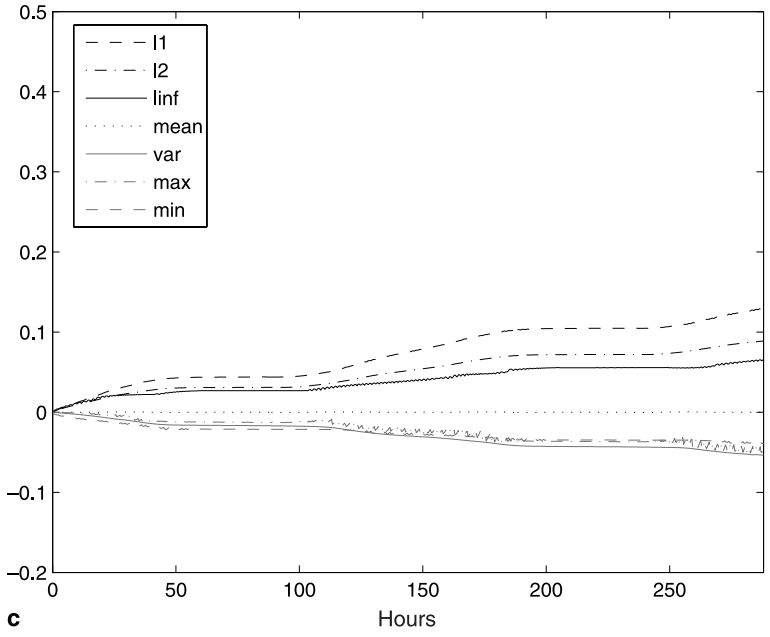

c

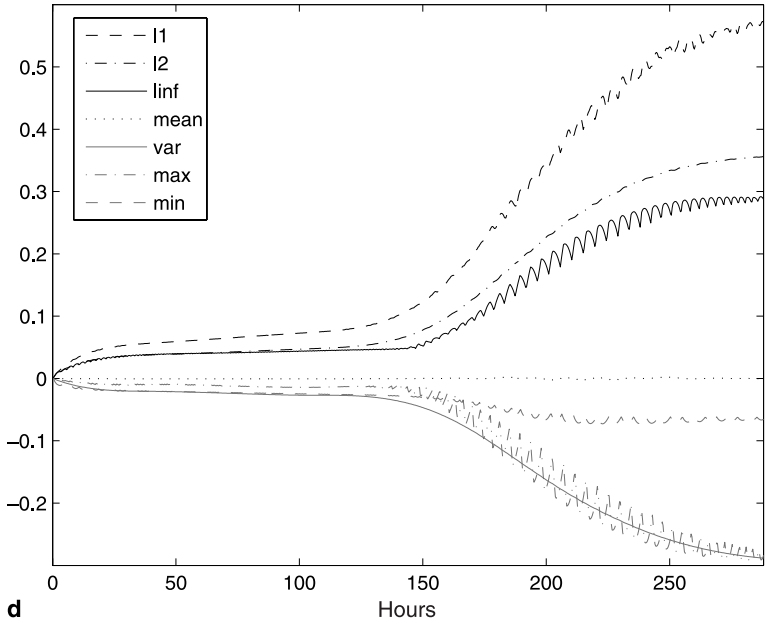

d

Fig. 12 (*continued*)

Integrations in the *diagonal* direction, that is, over the corners, revealed the problems that are already discussed in Sect. 3.1. Rotation at the variable resolution shows the similar improvement as the rotation in the normal direction.

3.3 Variable resolution on the octagonal grid

The octagonal grid is designed by a conformal mapping between two back-to-back octagons and a sphere (Purser and Rančić, 1997). There is more than one way to formulate the map space on the octagonal grid. Two basic topologies that are twisted versions of each other, A (with 14 panels) and B (with 28 panels) are shown respectively in Fig. 10.

The coordinate stretching on the octagonal grid can be applied only over the shaded panels in these figures, because the coordinate lines that are passing through other, non-shaded panels do not have a symmetrical position on two octagons that comprise the whole grid. For example, an x-coordinate on the left octagon that is close to the center converts into a y-coordinate close to the edge on the right octagon, and vice versa. Therefore, the topology B is probably better choice for

the application of grid stretching because of the larger area that could be used for stretching (24 out of 28 panels, that is, 85.71% of total domain, as opposed to 10 out of 14 panels, that is, 71.4% on topology A). Therefore, only topology B is used in this paper.

On the octagonal grid we compare the standard grid stretching against the Schmidt (1977) transformation. The uniform grid that is used in control tests has resolution of $19 \times 19 \times 28 = 10108$ grid points, which is a similar, though somewhat higher resolution than that on the uniform cubic grid.

The stretched grid is formulated in such a way that the area with the high resolution has the size of one panel, and is located at the center of each octagon, covering one quarter of each of the four central panels (see Fig. 10b). The rest of these four panels are used as the transitional regions. Outside of them the resolution is low and uniform in the direction normal to the sides of the octagons. We ran the cosine bell test with the couple of various stretching factors in order to estimate the effect of stretching, starting with the global stretching set to 2 (local stretching equal to 5.3%) and finishing with the global stretching set to 8 (local stretching equal to 9.6%). The octagonal stretched grid is shown in Fig. 11a.

The tests with the Schmidt transformation are run on the grid with the same number of grid points as the uniform grid. Within this method the two octagons are mapped asymmetrically onto the sphere, so that the one with the higher resolution occupies a smaller area (Fig. 11b). The stretching factor of the Schmidt transformation is 2.

In all of these tests (at the uniform, the grid-stretched and the Schmidt-transformed grid), the cosine bell starts at the edge of one of the octagons, passes through the centers of both octagons and returns back to the initial position after one full rotation. On the stretched grid, the cosine bell is going through two areas with the enhanced resolution, while on the Schmidt-transformed grid it goes through one area with the high- and one with the low-resolution. Evolution of diagnostic curves generated in these tests is shown in Fig. 12a–d.

The results on the uniform and stretched grid are very similar to those on the cubic grid. Further increase of the stretching factor improves the results (approximately up to value of 8.0), with the diagnostic curves flattening over the

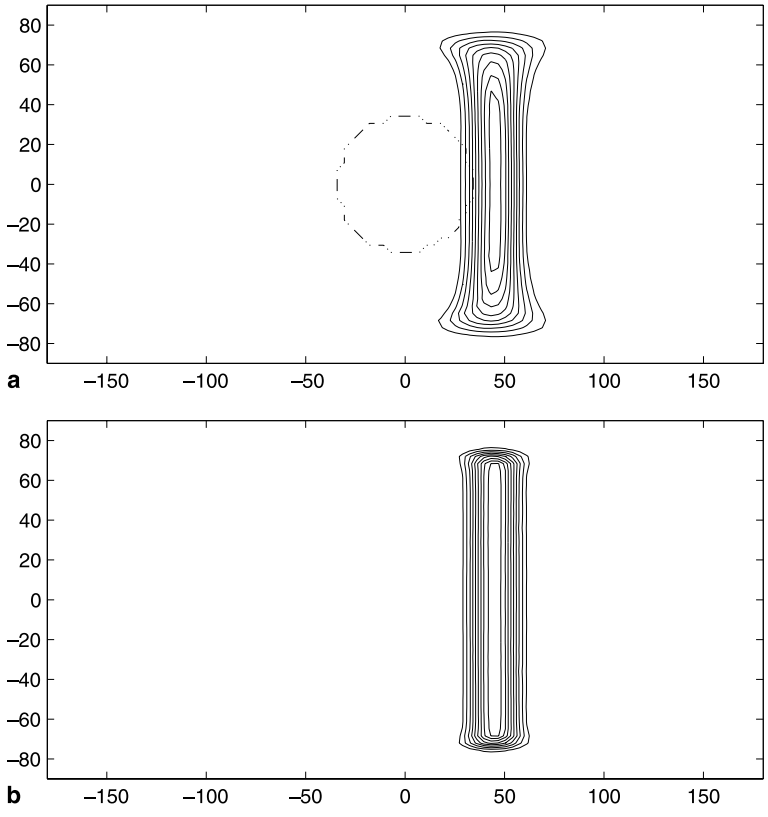

Fig. 13. Cosine wedge after 108 hours of integration on the octagonal grid with variable resolution (**a**) Schmidt transformation, (**b**) stretched grid

high resolution areas. However, the Schmidt transformation does not perform well in these tests. Although the errors over the high resolution area on the Schmidt transformed-grid are initially smaller than the errors on the uniform grid, they suddenly become much worse over the low resolution portion, which is about two times less resolved than the uniform grid.

Another drawback of the Schmidt transformation is the similar problem as the one encountered at the locally overlapped high-resolution domain described in 2D test on the plane. If the perturbation is large enough to pass simultaneously through both the high- and the low-resolution area, different portions of the perturbation will experience different dispersion errors, resulting in a strong distortion of the amplitude of the solution.

In order to illustrate this problem, we ran the rotational test with a wedge of the passive scalar on the Schmidt-transformed grid and the stretched grid, respectively. The stretching factor on the Schmidt-transformed grid is set to 3.3. The shape of the wedge after 108 hours of integration (just after it moves through the high-resolution region of the Schmidt-transformed grid) is shown in Fig. 13a. The outlined circle in the center is the high-resolution region (the smaller of two comprising octagons).

The wedge after 108 hours in the test on a stretched grid with an equivalent stretching factor of 3.3 (with local stretching of 7.5%) is shown in Fig. 13b. The octagons are now of the same size. The solution on the stretched grid preserves uniformity of the solution in the latitude. At the same time, it has generally smaller dispersion than the solution on the uniform grid (not shown here).

4. Discussion and conclusions

In this paper, we have investigated three different techniques as the candidates for introducing the variable resolution within the model operating on a rectangular, conformal, quasi-uniform grid. Based on the performance both in the plane and on the quasi-uniform grids, we concluded that the grid stretching is for now the most optimal choice for the task. The Schmidt-transformed grid and the local grid overlapping (version 1 in this paper) are completely eliminated from further considerations, because these two techniques show clearly inferior results in our tests. This is unfortunate, because both these grids have high versatility, low computing demands, and are relatively simple for implementation.

The version 2 of the grid overlapping showed the best results in our tests, but is for now put aside being too demanding in terms of computing memory and programming effort involved. However, we emphasize once again that, unlike the grid stretching, the grid overlapping preserves a local isotropy of the grid, and remains in the center of attention for some future study.

In Table 1, we calculate a relative efficiency of the methods for the variable resolution in comparison to the overall high resolution. We define this efficiency as the percentage rate of the number of grid points at the variable resolution normalized by the number of grid points at the global high resolution. We consider only the grid stretching and the consistent version 2 of the grid overlapping, which is derived by assuming that the common area on the overlapping grid has the same size as the transitional area on the stretched grid, and that the low and the high resolutions are the same as on the stretched grid. Calculations are done for the stretching factors ranging from 2 to 6. When the percentage rate is close to 100, the method requires similar amount of memory as the overall high resolution, and therefore becomes redundant. The smaller the percentage rate, the more favorable is situation in terms of saving the memory in comparison to the global high-resolution scenario.

Table 1. Percentage rate of the number of grid points at variable resolution normalized by the number of grid points at overall high resolution on the cubic and octagonal grids for different stretching factors

Stretching factor		2	3	4	5	6
Cubic	overlapped	66.67	44.30	34.67	29.39	26.07
	stretched	39.67	25.33	19.25	15.95	13.89
Octagonal	overlapped	83.93	62.70	53.13	47.71	44.25
	stretched	50.45	37.30	31.36	28.00	25.84

The results from Table 1 show that the grid stretching is systematically more efficient than the grid overlapping. The efficiency of both methods improves with the increase of the stretching factor. At the same time, the advantage of the grid stretching is becoming smaller. Both methods are more efficient on the cubic than on the octagonal grid.

All our tests have been done without artificial diffusion (or filtering) which is usually applied in the case of variable resolution in order to minimize the adverse effects of the internal reflection of waves caused by the irregularity of the grid (e.g., Vichnevetsky, 1987). Inclusion of such filtering may further improve the results. In principle, one can define a more sophisticated change of the grid interval in the transitional region of the stretched grid instead of the simple linear that is used in out tests. We indeed ran the preliminary tests using the nonlinear function from (11) to define the transitional region, but in the framework of our linear experiments, we did not notice any substantial improvement.

The suggested new technique for treatment of corners on the quasi-uniform grids successfully eliminates the problem previously observed in our tests. Part of the problem is related to the method of directional splitting used by the advection scheme in 2D case.

The new technique for handling corners introduces a small amount of overlapping of the faces, and consequently some computational overhead. In the case of linear advection, the overhead is really small and limited to a couple of grid points around the corners. For comparison, in the case of a full gnomonic cube of Ronchi et al (1995), overlapping and double calculations over the same areas may involve up to 20% of the computational domain, almost wiping out the benefits of the larger time-step. In our case the introduced modification actually improves (for about 40% in average) the grid aspect ratio, defined as the ratio between the grid distance of the smallest and the largest grid box. As an illustration, Fig. 14 shows the aspect ratios on the cubic and the octagonal grids before and after modification in function of resolution.

The introduced technique for handling the corners in the linear advection tests does not automatically guarantee conservation in remapping between the original and the modified grid. In principle, one can start this modification deeper inside the face, which may further improve the aspect ratio of the grid, but broaden the overlapping area between faces. Alternatively, one can apply the same technique on the ''smoothed'' versions of these grids (Purser and Rančić, 1998), which were introduced with the idea to increase uniformity of the quasi-uniform grids by relaxing the conformality constraint. In both cases the common area covered by the three neighboring faces would be much larger, and there would be need to apply higher order interpolations. A candidate for this task may be some

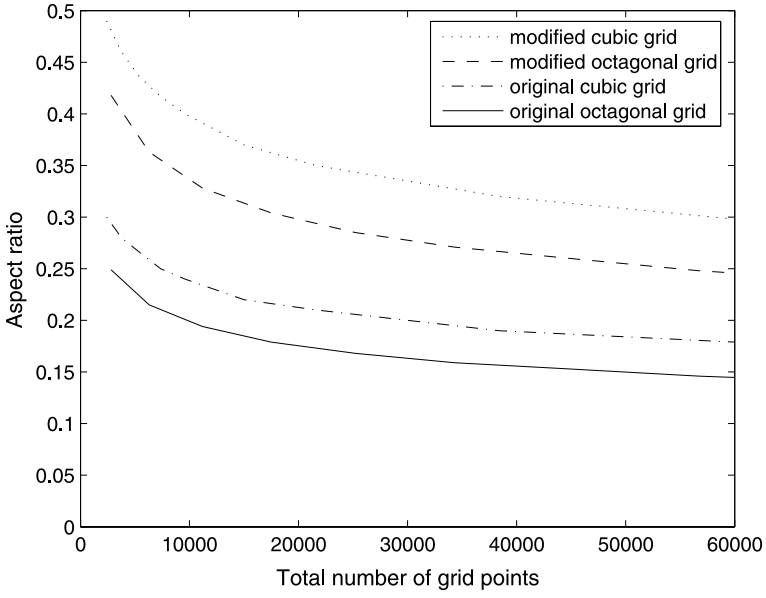

Fig. 14. Aspect ratio on the cubic and the octagonal grid before and after modification as function of resolution

variation of the cascade interpolations that would consist of a series of successive applications of a 1D interpolator. Beside computational efficiency, such an approach may have potential to maintain conservation of the interpolated variables along the line of ideas on conservative remapping suggested in the context of semi-Lagrangian framework (e.g., Rančić, 1995; Leslie and Purser, 1995; Zerroukat et al, 2002). However, the exploration of this issue is left for a future research.

In future, we intend to apply the grid stretching, first in the more complex test experiments, and then in the full 3D model.

Appendix

Some more details about the corner problem on the quasi-uniform grids

Corner points introduce two major problems

The first of them is explained with the aid of Fig. 15. When updating values at the grid points located close to the corners, the *x*- and *y*-directional fluxes may actually come not from the normal directions, like in the rest of the domain, but rather from almost parallel directions! As schematically shown in Fig. 15, when perturbation is coming from the edge between the faces B and C, it is actually taken into account twice in calculations at the grid box located in the corner of the face A. This explains some of the sudden overshoots from the regular pattern revealed by the diagnostics in Fig. 5.

The second effect that contributes to the bumpiness of diagnostics is a well known problem of splitting. Grid boxes located next to the corners lose parallelism of their opposing sides. The divergence in one direction is proportional to the difference between normal wind components at two opposing sides of this box. Since these sides are not parallel to each other, the divergence is not equal to zero, even if the flow is constant and non-divergent. The same applies to the other direction. Thus, the grid geometry by itself falsely generates the divergence in each pass. (Note however, that if a full 2D scheme, that does not need the directional splitting, is applied, the divergence would be equal to zero, because the errors from both directions would exactly compensate each other).

The new method for treatment if singular points successfully eliminates both of these problems.

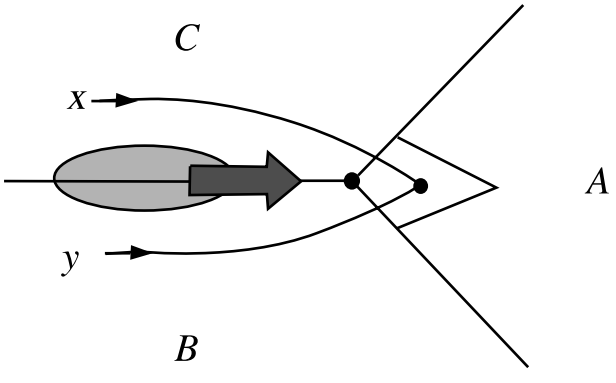

Fig. 15. Mechanism of overshoots in the diagnostics (see text for details)

Acknowledgements

The work on this project was sponsored by the National Science Foundation (Award no. ATM-0113037). The project was executed using the high-performance computing facilities and other resources at NASA's Goddard Space Flight Center (GSFC), through collaboration with the University of Maryland, Baltimore County (UMBC), and the Beowulf cluster at the Department of Mathematics and Statistics of UMBC. The authors are grateful to James Fischer form GSFC, Dr. Bob Curran former Director of the Goddard Earth Science and Technology Center, and Dr. Ray Hoff, the Director of Joint Center for Earth Systems Technology for the support during work on this project. We would also like to express our gratitude to Prof. Matthias Gobbert and Prof. Wallace McMillan from UMBC for their support. Special thanks to Dr. Fox-Rabinovitz for encouragement and many instructive discussions, and Dr. Sushel Unninayar for reading early drafts of this manuscript and making a number of valuable comments. The authors are also indebted to the unknown reviewers of the previous version of the paper for their helpful and constructive comments.

References

Adcroft A, Campin J-M, Hill C, Marshall J (2004) Implementation of an atmosphere-ocean general circulation model on the expanded spherical cube. Mon Wea Rev 132: 2845–2863

Baumgardner JR, Frederickson PO (1985) Icosahedral discretization of the two-sphere. SIAM J Sci Comp 22: 1107–1115

Browning GL, Hack JJ, Swarztrauber PN (1989) A comparison of three numerical methods for solving differential equations on the sphere. Mon Wea Rev 117: 1058–1075

Chesshire G, Henshaw WD (1990) Composite overlapping meshes for the solution of partial differential equations. J Comput Phys 90: 1–64

Côté J, Roch M, Staniforth A, Fillon L (1993) A variable-resolution semi-Lagrangian finite-element global model of the shallow-water equations. Mon Wea Rev 121: 231–243

Deque M, Piedelievre JP (1995) High resolution climate simulation over Europe. Climate Dyn 11: 321–339

Fletcher CAJ (1991) Computational techniques for fluid dynamics, 2nd ed. Springer, 493 pp

Fox-Rabinovitz MS (2000) Simulation of anomalous regional climate events with a variable-resolution stretched-grid GCM. J Geophys Res 105: 29,635–29,645

Fox-Rabinovitz MS, Takacs LL, Govindaraju RC, Suarez MJ (2001) A variable resolution stretched-grid general

circulation model: regional climate simulation. Mon Wea Rev 129: 453–469

Heikes RP, Randall DA (1995a) Numerical integration of the shallow-water equations on a twisted icosahedral grid. Part I: basic design and results of tests. Mon Wea Rev 123: 1862–1880

Heikes RP, Randall DA (1995b) Numerical integration of the shallow-water equations on a twisted icosahedral grid. Part II: a detailed description of the grid and an analysis of numerical accuracy. Mon Wea Rev 123: 1881–1887

Leslie LM, Purser RJ (1995) Three-dimensional mass-conserving semi-Lagrangian scheme employing forward trajectories. Mon Wea Rev 123: 2551–2566

Majewski D, Liermann D, Prohl P, Ritter B, Buchhold M, Hanisch T, Paul G, Wergen W, Baumgardner J (2002) The operational global icosahedral-hexagonal gridpoint model GME: description and high-resolution tests. Mon Wea Rev 130: 319–338

McGregor JL (1997) Semi-Lagrangian advection on a cubic gnomonic projection of the sphere. In: Numerical methods in atmospheric and oceanic modelling (Lin C, Laprise R, Ritchie H, eds). Canadian Meteorological and Oceanic Soc./NRC Research Press, pp 153–169

Mesinger F, Arakawa A (1976) Numerical methods used in atmospheric models. WMO, GARP Publ. Ser. 17, Vol. I, 64 pp

Ničković S (1994) On the use of hexagonal grids for simulation of atmospheric processes. Contr Atmos Phys 67: 103–107

Ničković S, Gavrilov MB, Tošić IA (2002) Geostrophic adjustment on hexagonal grids. Mon Wea Rev 130: 668–683

Phillips NA (1959) Numerical integration of the primitive equations on the hemisphere. Mon Wea Rev 87: 333–345

Purser RJ, Rančić M (1997) Conformal octagon: an attractive framework for global models offering quasi-uniform regional enhancement of resolution. Meteorol Atmos Phys 62: 33–48

Purser RJ, Rančić M (1998) Smooth quasi-homogeneous gridding of the sphere. Quart J Roy Meteor Soc 124: 637–647

Rančić M (1995) An efficient, conservative, monotonic remapping for semi-Lagrangian transport algorithms. Mon Wea Rev 123: 1213–1217

Rančić M, Purser RJ, Mesinger F (1996) A global shallow water using and expanded spherical cube: gnomonic versus conformal coordinates. Quart J Roy Meteor Soc 122: 959–982

Randall D, Curry J, Battisti D, Flato G, Grumbine R, Hakkinen S, Martinson D, Preller R, Walsh J, Weatherly J (1988) Status and outlook for large scale modeling of atmosphere-ice-ocean interactions in the Arctic. Bull Amer Meteor Soc 79: 197–219

Ronchi C, Iaccono R, Paolucci PS (1996) The ''cubed sphere'': a new method for the solution of partial differential equations in spherical geometry. J Comput Phys 124: 93–114

Sadourny R (1972) Conservative finite-differencing approximations of the primitive equations on quasi-uniform spherical grids. Mon Wea Rev 100: 93–144

Sadourny R, Arakawa A, Mintz Y (1968) Integration of the nondivergent barotropic vorticity equation with an icosahedral-hexagonal grid for the sphere. Mon Wea Rev 96: 351–356

Schmidt F (1977) Variable fine mesh in spectral global models. Contr Atmos Phys 50: 211–217

Straius G (1980) On composite mesh difference methods for hyperbolic difference equations. Numer Math 35: 241–255

Strang G (1968) On the construction and comparison of difference schemes. SIAM J Numer Anal 5: 506–517

Takacs LL (1985) A two-step scheme for the advection equation with minimized dissipation and dispersion errors. Mon Wea Rev 113: 1050–1065

Takle ES, Gutowski WJ Jr, Arritt RW, Pan Z, Anderson CJ, Silva R, Caya D, Chen S-C, Christensen JH, Hong S-Y, Juang H-MH, Katzfey JJ, Lapenta WM, Laprise R, Lopez P, McGregor J, Roads JO (1999) Project to Intercompare Regional Climate Simulations (PIRCS): description and initial results. J Geophys Res 104: 19,443–19,462

Taylor M, Tribbia J, Iskandarni M (1997) The spectral element method for the shallow water equations on the sphere. J Comput Phys 130: 92–108

Tomita H, Satoh M, Goto K (2002) An optimization of the icosahedral grid modified by spring dynamics. J Comput Phys 183: 307–331

Vichnevetsky R (1987) Wave propagation and reflection in irregular grids for hyperbolic equations. Appl Numer Math 2: 133–166

Williamson DL (1970) Integration of the primitive barotropic model over a spherical geodesic grid. Mon Wea Rev 98: 512–520

Williamson DL, Drake JB, Hack JJ, Jakob R, Swarztrauber PN (1992) A standard test set for numerical approximations to the shallow water equations in spherical geometry. J Comp Phys 102: 211–224

Zerroukat M, Wood N, Staniforth A (2002) SLICE: a semi-Lagrangian inherently conserving and efficient scheme for transport problems. Quart J Roy Meteor Soc 128: 2801–2820

Corresponding author's address: Miodrag Rančić, UMBC/JCET, Academic IV, Room 114K, 1000 Hilltop Circle, Baltimore, MD 21250, USA (E-mail: mrancic@umbc.edu)